Supplementary Materials

Defect-engineered Ru-Co/TiO_{2-x} catalysts for highly efficient plasma-catalytic ammonia synthesis at ambient conditions

Bianbian Gao [a,b], Yutong Feng [a,b], Chunyu Li [a], Jiantao Zhao [a], Yitian Fang [a], Guoqiang Cao [a,*]

[a] State Key Laboratory of Coal Conversion, Institute of Coal Chemistry, Chinese Academy of Sciences, Taiyuan 030001, China

[b] University of Chinese Academy of Sciences, Beijing 100049, China

*Corresponding author: caoguoqiang@sxicc.ac.cn

1. **Experimental details**

The DBD reactor employs a quartz tube (inner diameter 20 mm, outer diameter 24 mm) as the dielectric barrier layer, around whose outer wall a meshed stainless-steel wire serving as the grounding electrode is wound, with an effective discharge length of 150 mm. Inner quartz electrode rods (outer diameter 14 mm) are placed along the axis of the quartz tube as high-voltage electrodes, with a discharge gap of 3 mm. A sinusoidal high-voltage power supply (Suman, CTP-2000KP) was used to apply voltage, generating discharge plasma within the quartz tube. The working frequency was approximately 9.6 kHz. After capacitive voltage division (ratio 1:1000), the voltage at both ends of the reactor was measured using an inductive voltage probe (Tektronix, TPP0201). All electrical signals were collected by a dual-channel digital oscilloscope (Tektronix, TBS1102C). The discharge power was calculated by integrating the area of the Q-U Lissajous figure. To reduce digital image noise, the electrical signals required for drawing the Lissajous figure were processed through three averaging samplings. The exhaust gas after the reaction enters the chemical absorption device to capture the generated NH_3.

Typically, 100 mg catalysts were fixed in the gap between the high voltage electrode and the quartz tube. N_2 and H_2 were transported to the packed DBD plasma reactor in a certain proportion. Under the synergistic action of the catalyst, energy was input into the reaction system through alternating current power supply to conduct the ammonia synthesis reactions. The configured 0.005 $mol \cdot L^{-1}$ dilute H_2SO_4 solution absorption device was used to absorb and detect the NH_3.

2. Supporting Figures and Tables

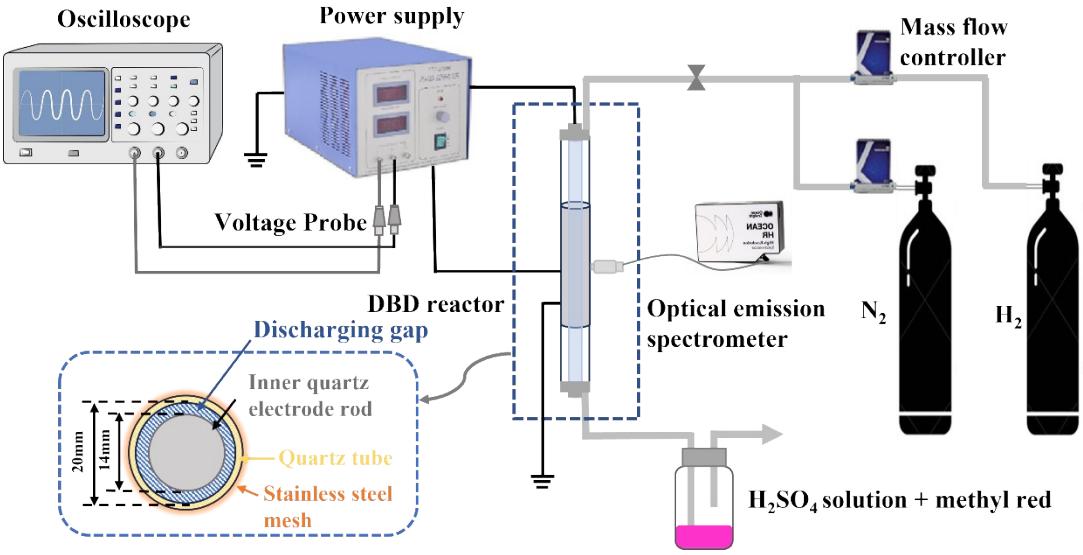

Fig. S1 Schematic diagram of the plasma-catalytic NH_3 synthesis reaction system.

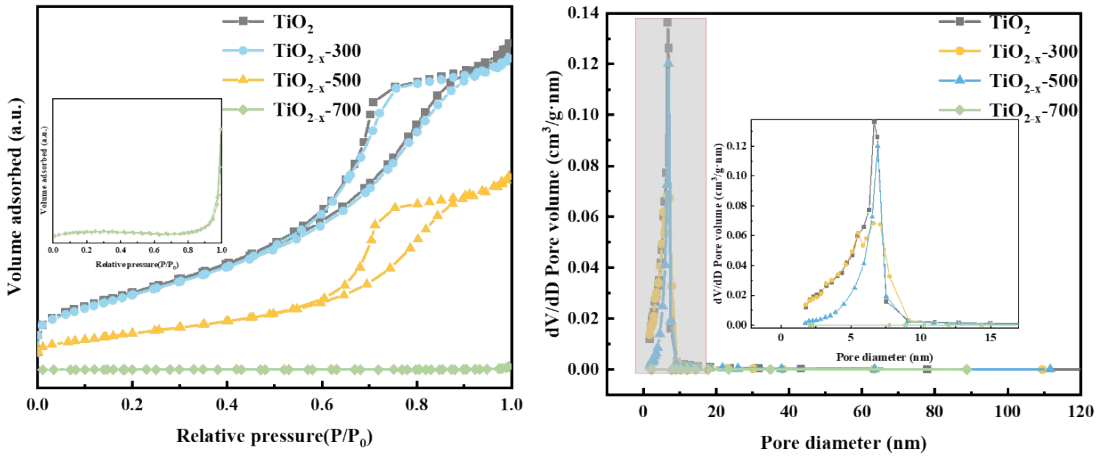

Fig. S2 (a) N_2 adsorption-desorption isotherms, (b) Pore size distribution curves of TiO_{2-x}-z supports.

Table S1 Physical properties of TiO_{2-x}-z supports and Ru-Co/TiO_{2-x}-z catalysts.

Samples	Specific surface area ($m^2 \cdot g^{-1}$)	Pore volume ($cm^3 \cdot g^{-1}$)	Average pore size (nm)	Anatase (%)[a]
TiO_2	175.99	0.318	5.48	87.1
TiO_{2-x}-300	171.71	0.303	5.31	86.3
TiO_{2-x}-500	81.92	0.187	6.63	89.7
TiO_{2-x}-700	0.68	0.003	38.86	1.2
Ru-Co/TiO_2	22.87	0.162	23.37	19.5
Ru-Co/TiO_{2-x}-300	20.24	0.164	27.40	19.1
Ru-Co/TiO_{2-x}-500	29.47	0.126	13.24	73.9
Ru-Co/TiO_{2-x}-700	4.27	0.033	30.19	1.7

[a] Anatase(%) was calculated by XRD:

Anatase%=$I_{anatase(101)}/(I_{anatase(101)}+1.4I_{rutile(110)})*100$.

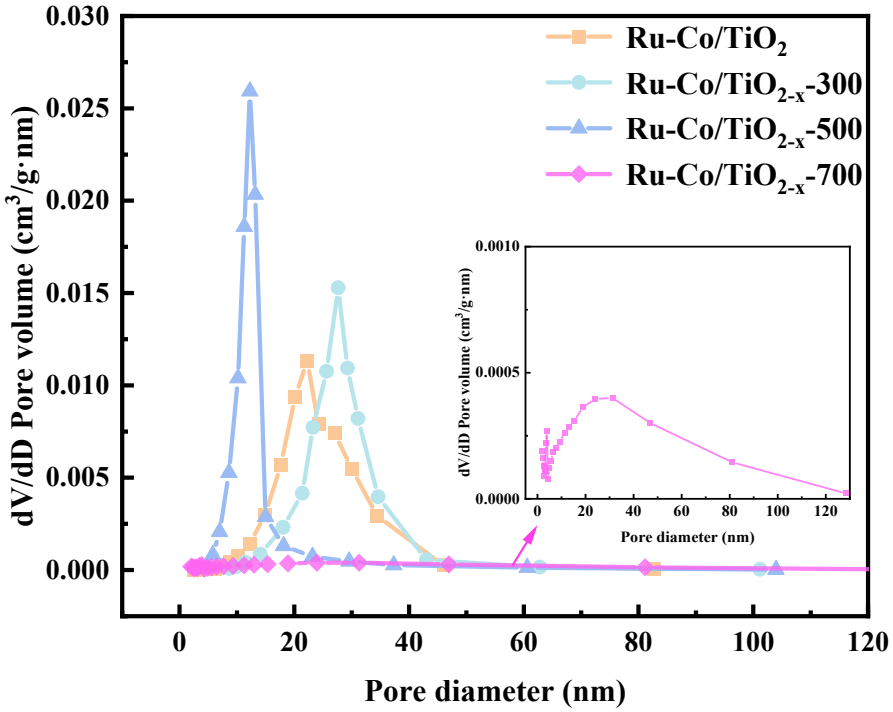

Fig. S3 Pore size distribution curves of Ru-Co/TiO_{2-x}-z catalysts.

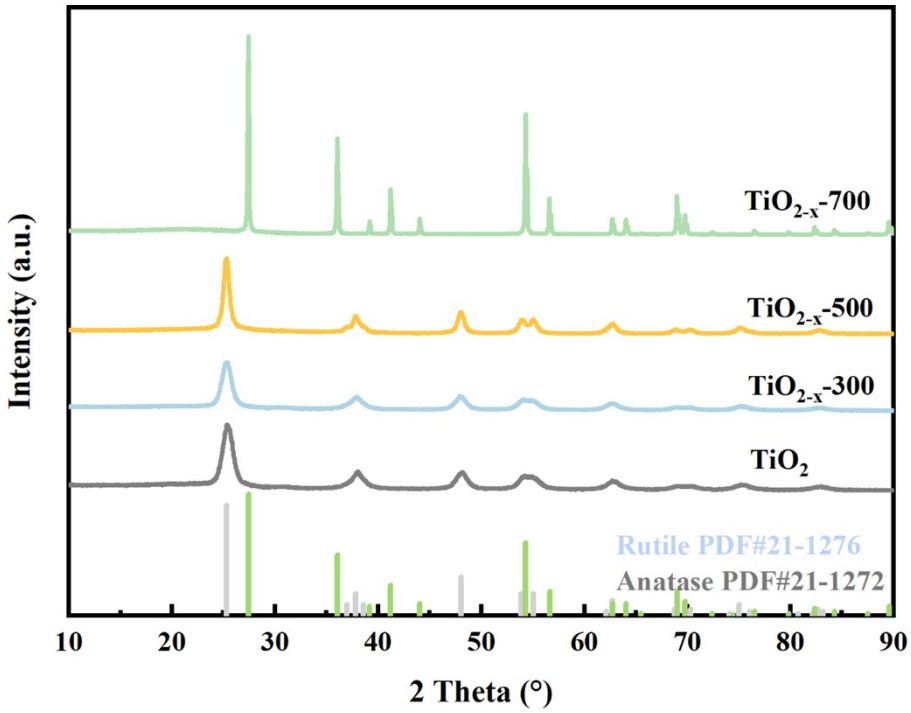

Fig. S4 XRD pattern of TiO_{2-x}-z supports.

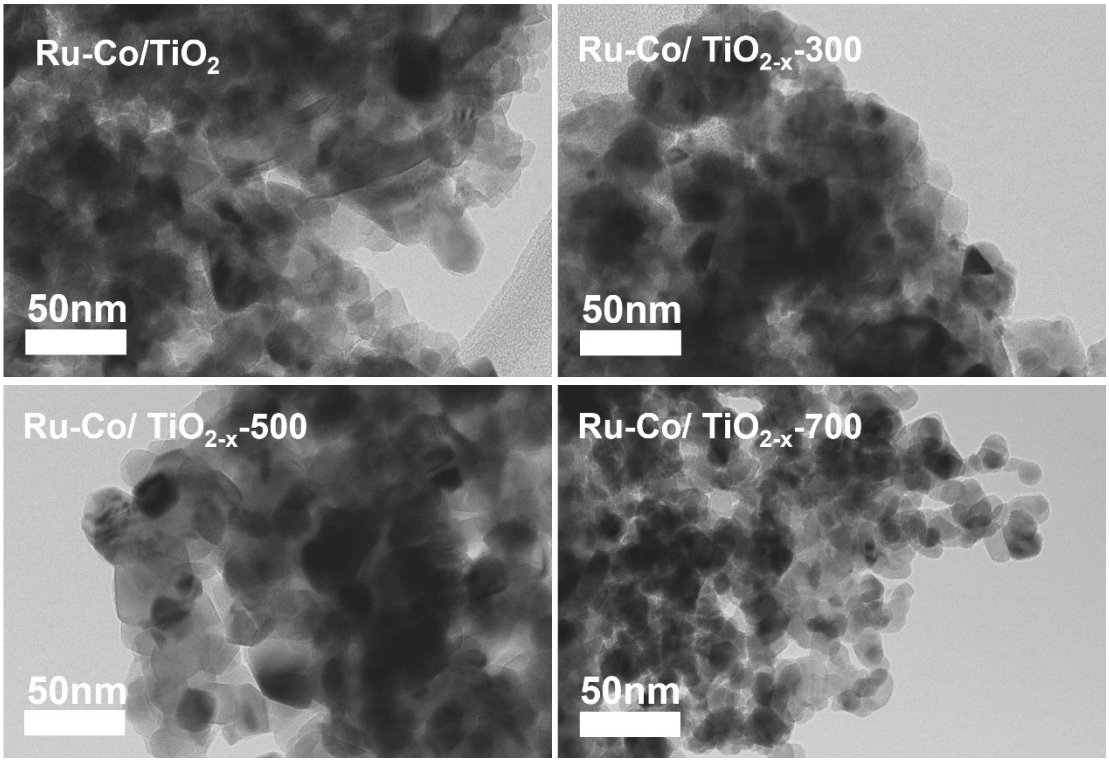

Fig. S5 HRTEM images of Ru-Co/TiO_{2-x}-z catalysts.

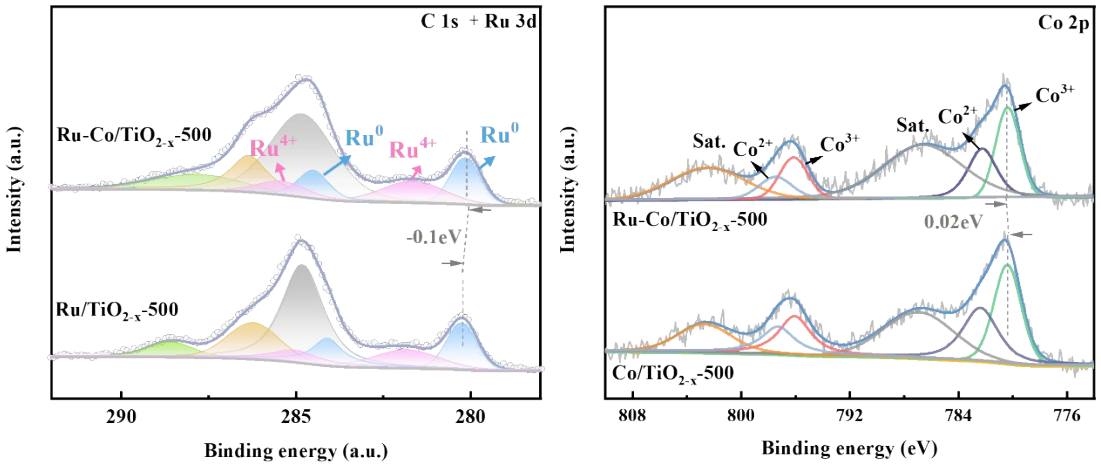

Fig. S6 XPS spectra comparison of (a) Ru 3d spectra for Ru/TiO_{2-x}-500 and Ru-Co/TiO_{2-x}-500 catalysts, (b) and Co 2p spectra for Co/TiO_{2-x}-500 and Ru-Co/TiO_{2-x}-500 catalysts.

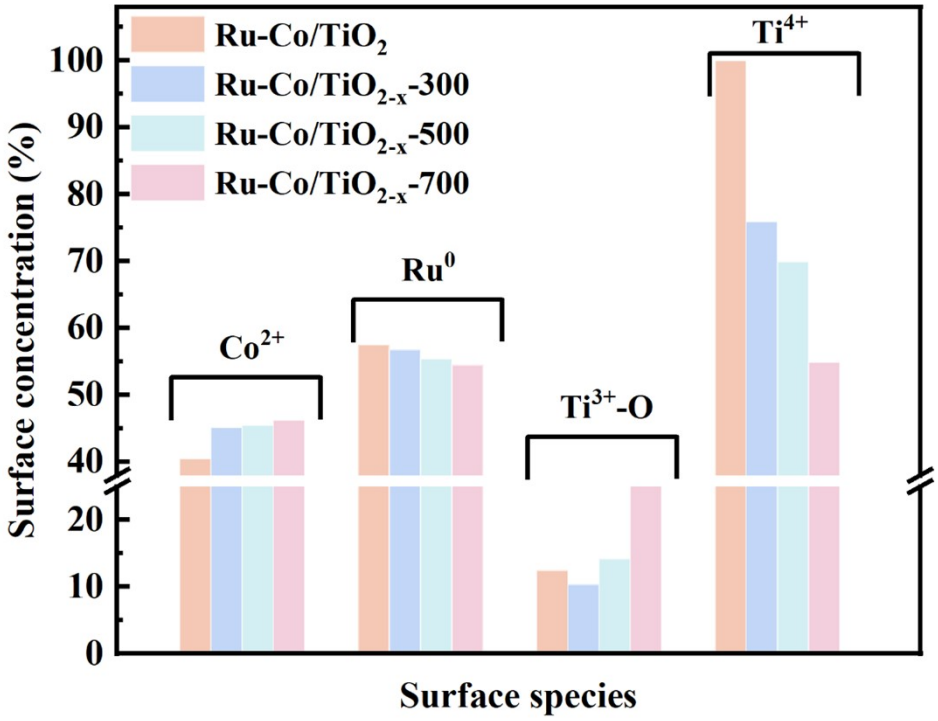

Fig. S7 Concentrations of Ru^0, Co^{2+}, oxygen species (Ti^{3+}-O) and Ti^{4+} on the catalyst surface based on the Ru 3d, Co 2p, O 1s and Ti 2p XPS spectra of Ru-Co/TiO_{2-x}-z catalysts.

Table S2 Quantitative Analysis of Co 2p, Ru 3d, O 1s, and Ti 2p Orbitals of Ru/TiO_{2-x}-500, Co/TiO_{2-x}-500 and $Ru\text{-}Co/TiO_{2-x}$-z Catalysts.

Catalysts	Co species(%)		Ru species(%)		Oxygen species(%)			Ti species(%)	
	Co^{2+}	Co^{3+}	Ru^{0}	Ru^{4+}	Ti-OH	Ti^{3+}-O	Ti^{4+}-O	Ti^{4+}	Ti^{3+}
Ru/TiO_{2-x}-500	-	-	54.5	45.4	5.4	8.8	86.5	-	-
Co/TiO_{2-x}-500	44.3	55.7	-	-	8.8	13.4	76.7	-	-
$Ru\text{-}Co/TiO_2$	40.5	59.5	53.2	46.8	24.8	10.4	64.8	100	-
$Ru\text{-}Co/TiO_{2-x}$-300	45.1	54.9	53.3	46.7	11.8	11.2	77.0	75.9	24.1
$Ru\text{-}Co/TiO_{2-x}$-500	45.5	54.5	55.2	44.8	12.5	13.4	74.1	69.9	30.1
$Ru\text{-}Co/TiO_{2-x}$-700	46.2	53.8	56.3	43.7	22.4	30.9	46.6	53.3	34.6

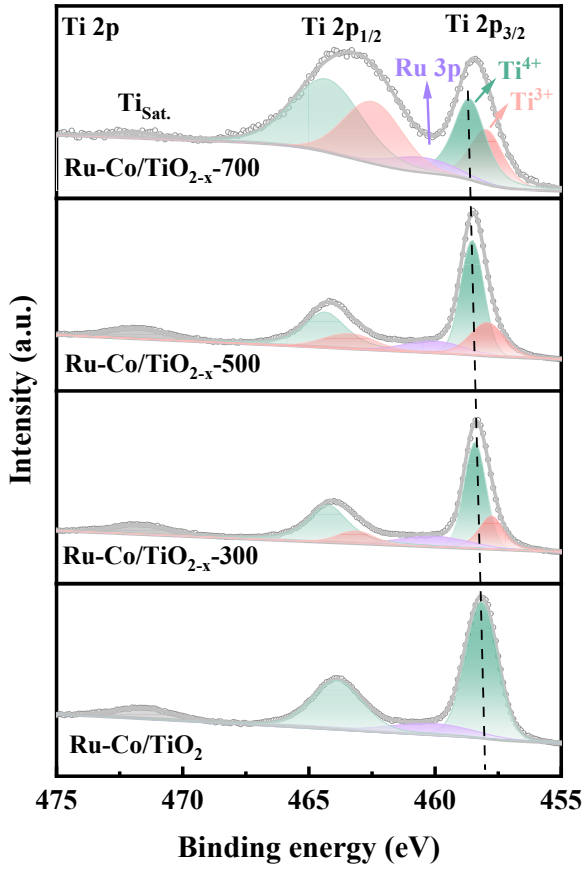

Fig. S8 Ti 2p XPS spectra of Ru-Co/TiO_{2-x}-z catalysts.

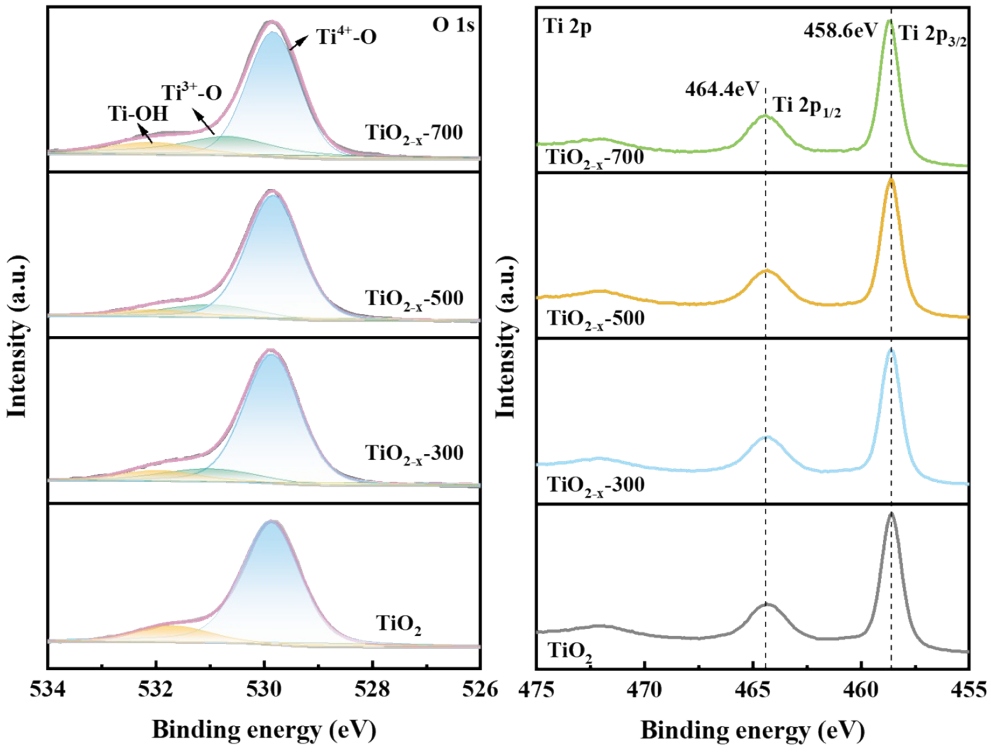

Fig. S9 XPS spectra of TiO_{2-x}-z (a) O 1s (b) Ti 2p.

Table S3 Quantitative Analysis of O 1s Orbitals of TiO_{2-x}-z samples.

Samples	Ti-OH	Ti^{3+}-O	Ti^{4+}-O
TiO_2	11.3%	-	88.7%
TiO_{2-x}-300	6.8%	10.6%	82.6%
TiO_{2-x}-500	5.9%	11.3%	82.8%
TiO_{2-x}-700	9.2%	24.2%	66.6%

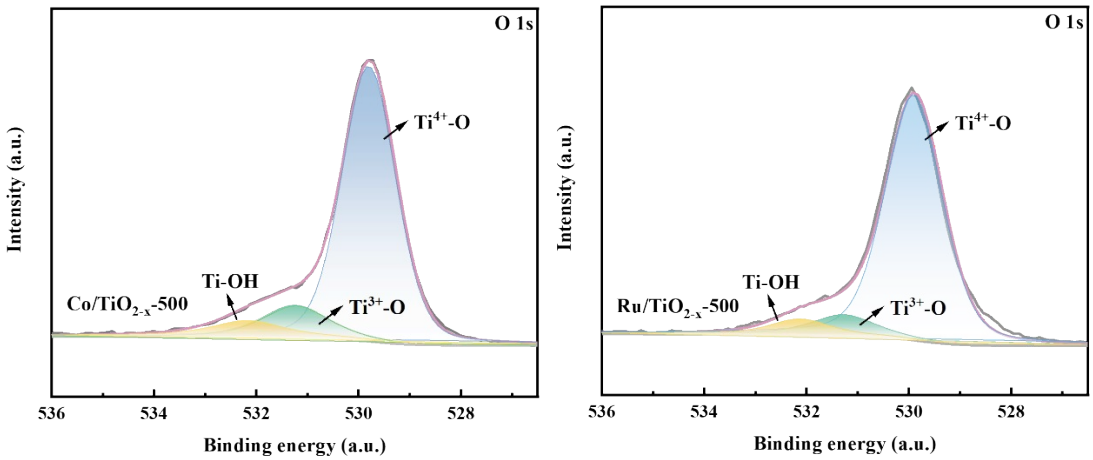

Fig. S10 High-resolution XPS peaks of O 1s spectra for (a) Co/TiO_{2-x}-500, and (b) Ru/TiO_{2-x}-500 catalysts.

Table S4 The surface basicity of Ru-Co/TiO_{2-x}-z catalysts.

Samples	CO_2 desorption (mmol·g^{-1})
Ru-Co/TiO_2	0.521
Ru-Co/TiO_{2-x}-300	0.439
Ru-Co/TiO_{2-x}-500	0.488
Ru-Co/TiO_{2-x}-700	0.302

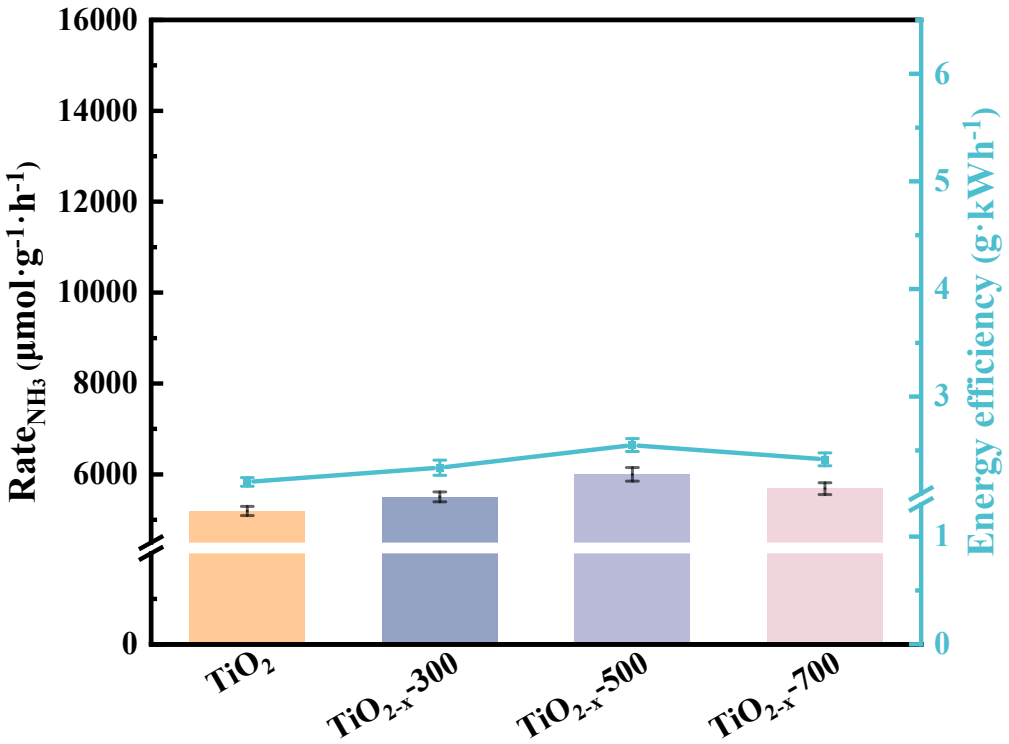

Fig. S11 NH_3 synthesis rate and energy efficiency over pure TiO_{2-x}-z supports.

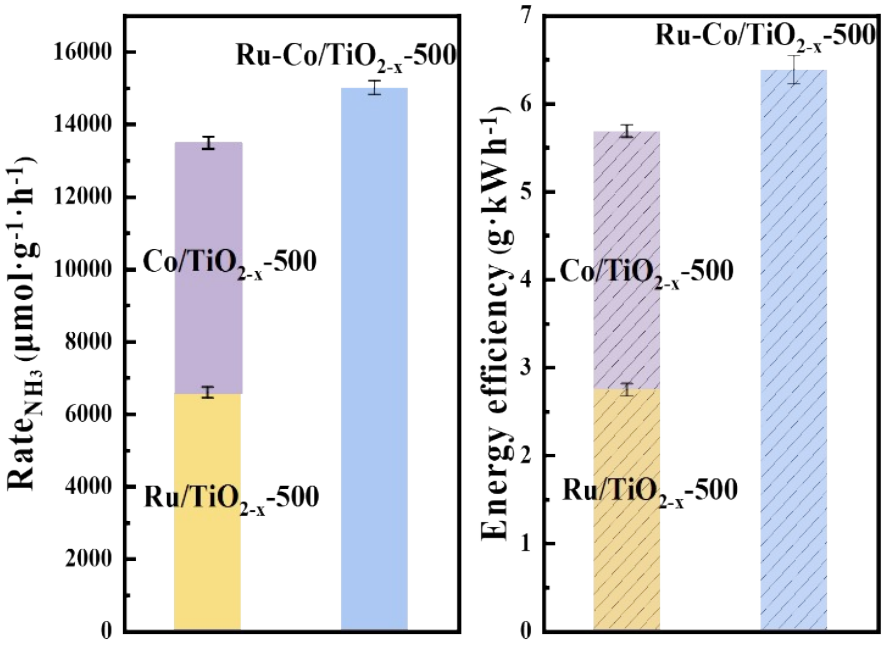

Fig. S12 NH_3 synthesis rate and energy efficiency over Ru/TiO_{2-x}-500 and Co/TiO_{2-x}-500 catalysts.

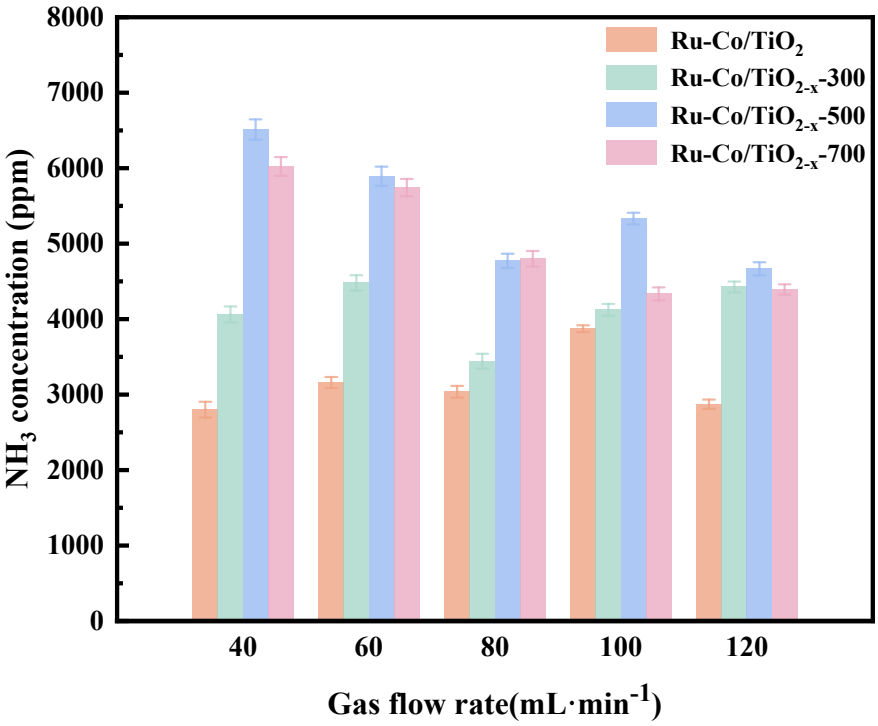

Fig. S13 NH_3 concentration over Ru-Co/TiO_{2-x}-z catalysts at various total gas flow rates.

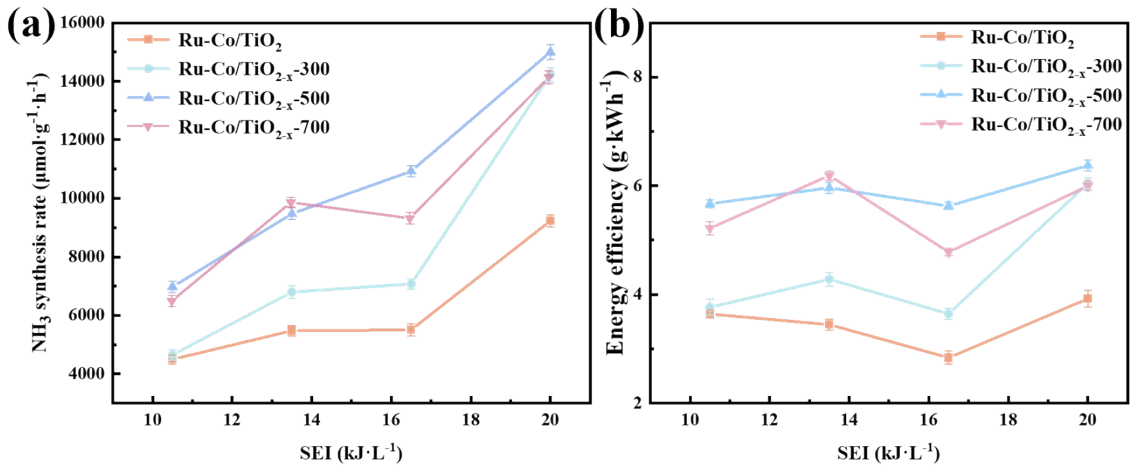

Fig. S14 (a) NH_3 synthesis rate and (b) Energy efficiency over Ru-Co/TiO_{2-x}-z catalysts at various SEI (at a fixed flow rate of 120 mL·min^{-1}).

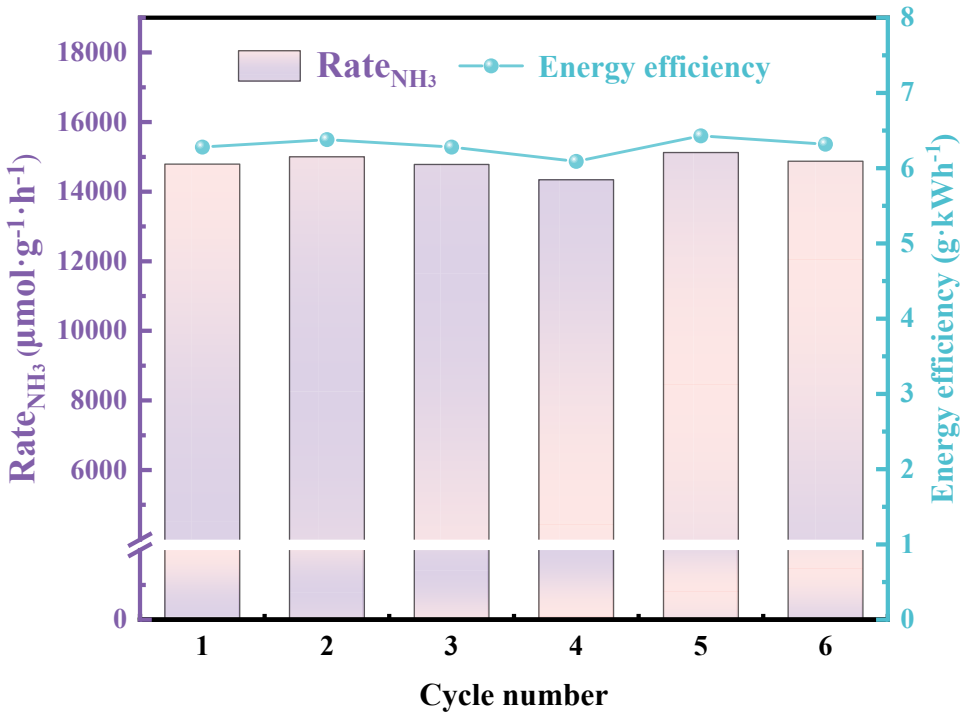

Fig. S15 The stability tests of Ru-Co/TiO_{2-x}-500 catalysts for 6 cycles.

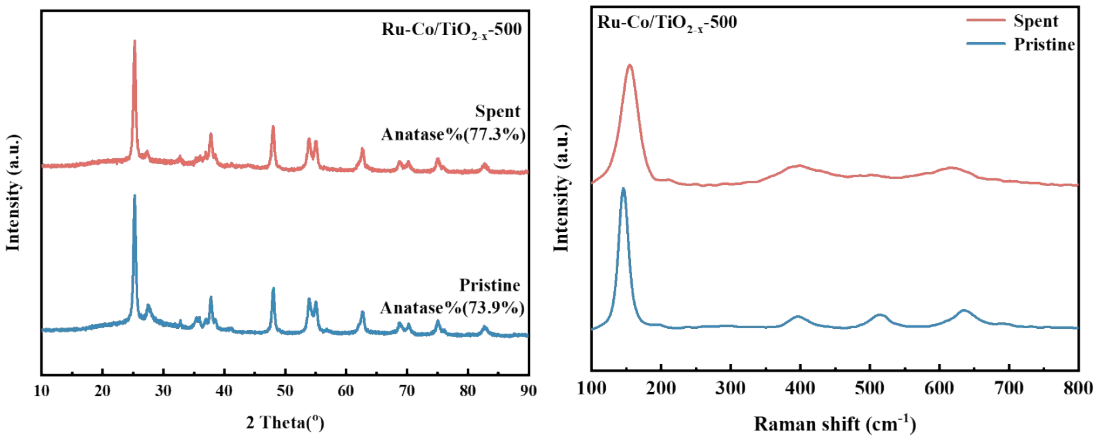

Fig. S16 (a) XRD pattern of pristine and spent Ru-Co/TiO_{2-x}-500 catalysts. (b) Raman spectra of pristine and spent Ru-Co/TiO_{2-x}-500 catalysts.

Table S5 Performance comparison of recently reported plasma-catalytic ammonia synthesis catalysts in DBD reactors at atmospheric pressure.

Catalysts	Discharge parameters			Reaction conditions			SEI ($kJ \cdot L^{-1}$)	$Rate_{NH3}$ ($\mu mol \cdot g^{-1} \cdot h^{-1}$)	EE ($g_{NH3} \cdot kWh^{-1}$)
	f (kHz)	U (kV)	P (W)	N_2/H_2	Q_{gas} ($mL \cdot min^{-1}$)	T (^oC)			
SBA-15[1]	8.0	7.5-9.5	(Input) 100	1:1	20	-	-	5337	1.04
VN[2]	10	-		2:3	100	100	-	8423	1.43
Co/BCN[3]	-	-	-	1:3	40	75	-	2478	2.09
Co/SiO_2[4]			2	N_2+H_2O	6.2	122-144	19	3700	3.20
Co SACs[5]	-	-	59	2:3	25	-	142	10647	0.31
Co-Ni/MOF-74[6]	-	-	35	1:1	200	-	11	2609	0.72
Ru/α-Al_2O_3[7]	-	-	38	2:1	120	-	19	1186	1.89
Ru/Al_2O_3 membrane[8]	21.5	-	127	1:3	30	-	254	960	0.37
Ru/LDH-*P*[9]	8.1	12	13	1:1	20	-	39	4500	1.70
Ru-Mg/Al_2O_3[10]			1200	4:1	2000	300	36	565	35.70
Ru-Co/AC[11]	-	-	40	1:1	120	-	20	7547	3.21
Ru-Co/TiO_{2-x}-500 (This work)	-	-	40	1:1	120	-	20	15000	6.38

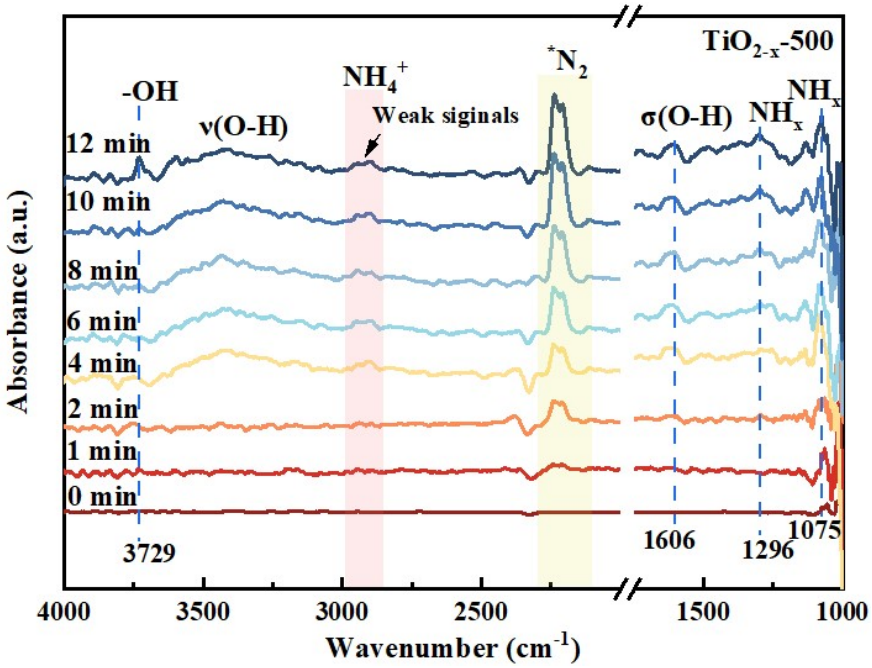

Fig. S17 In-situ DRIFTS spectra of plasma-catalytic NH_3 synthesis over pure TiO_{2-x}-500 support.

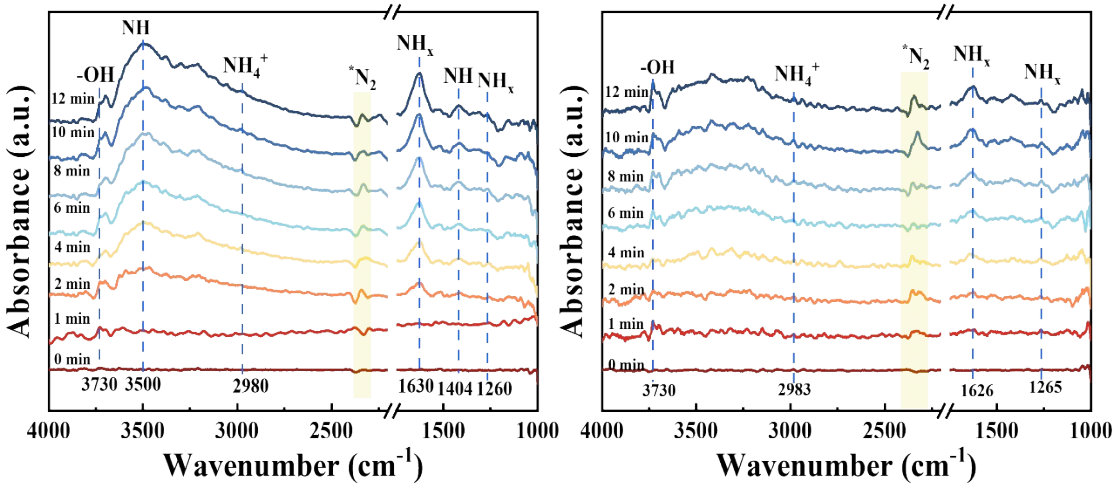

Fig. S18 In-situ DRIFTS spectra of plasma-catalytic NH_3 synthesis over (a) Co/TiO_{2-x}-500 (b) and Ru/TiO_{2-x}-500 catalysts.

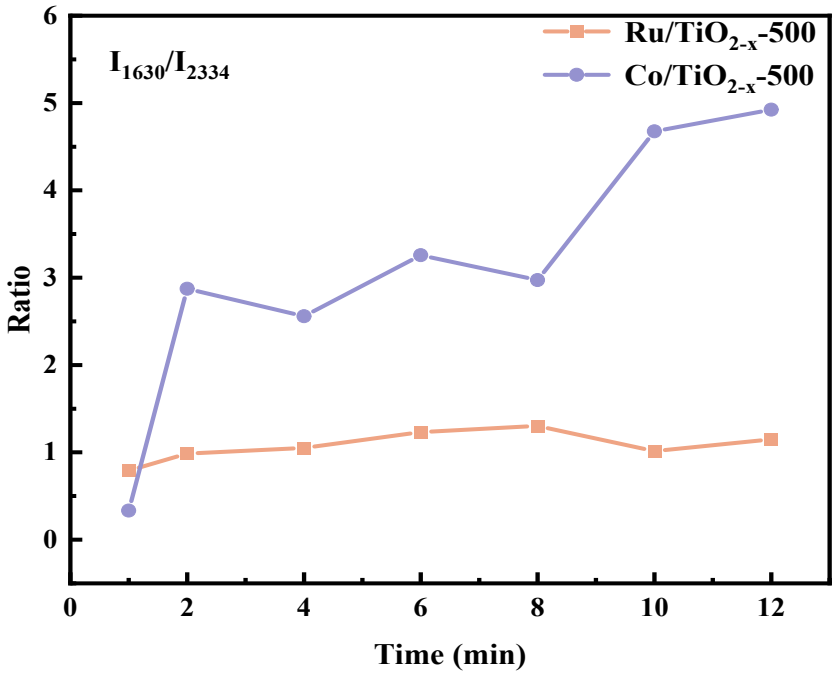

Fig. S19 The characteristic peak intensity ratios (1630 cm^{-1}/2334 cm^{-1}, $^*NH_x/^*N_2$) of intermediate species during plasma-catalytic ammonia synthesis over Ru/TiO_{2-x}-500 and Co/TiO_{2-x}-500 catalysts.

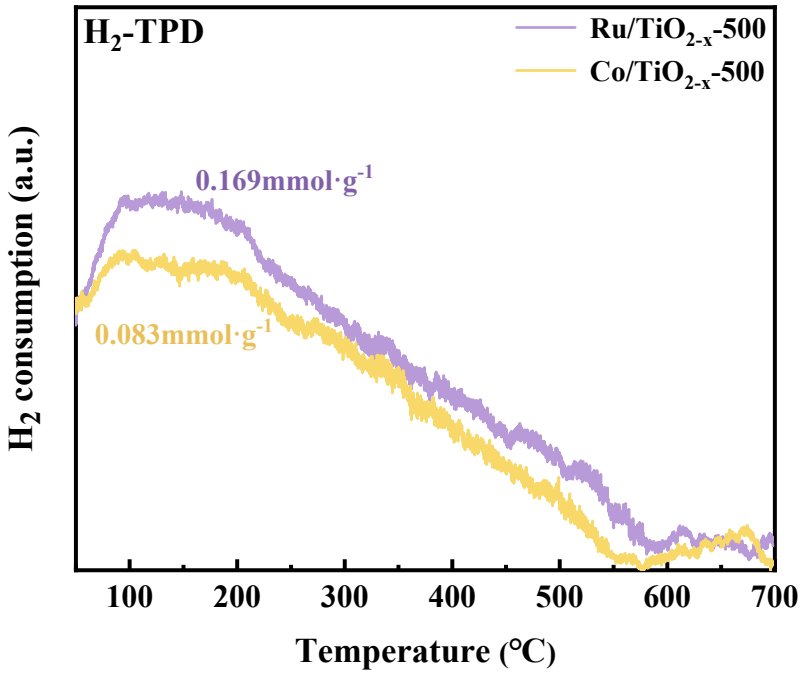

Fig. S20 H_2-TPD profiles of Ru/TiO_{2-x}-500 and Co/TiO_{2-x}-500.

Table S6. Summary of vibrational peak assignments for adsorbed species on catalyst surfaces.

Absorbed specie	Vibrational peak (cm^{-1})	Assignment	Literature value
NH_4^+/NH_3	2980, 2896	NH_4^+	2980, 2890[12,13], 2894[14]
NH_x	1055	N-H	1056[14]
	1400,1404	NH deformation	1392[14], 1427, 1414, 1440[15]
	1238,1296	H-N-H bending of NH_x species	1238[14], 1242[14]
	1558 (NH_2)	-NH_2 wagging	1531[16], 1535, 1543[17]
	1638,1640	δ_{as} (NH_3)	1639, 1644[18], 1620, 1628
$^*N_2$	2212	N-N stretching	2241, 2250, 2268[17]
	2169,2334		2100-2300[17]

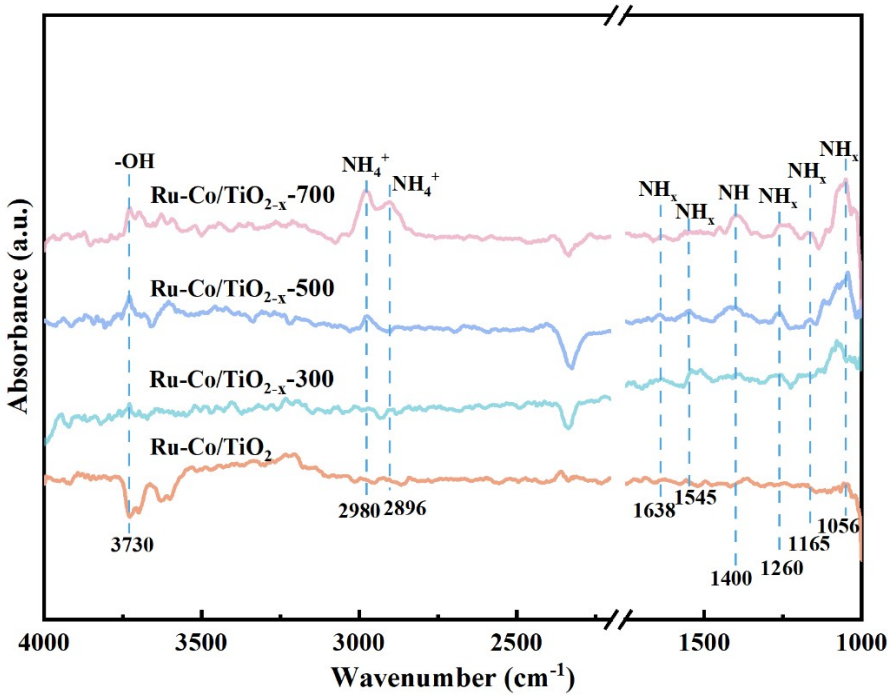

Fig. S21 In-situ DRIFTS spectra of plasma-catalytic NH_3 synthesis over Ru-Co/TiO_{2-x}-z catalysts. (Discharge time = 6 min)

3. **Theoretical calculations methods**

Density functional theory (DFT) calculations were performed using the Vienna Ab initio Simulation Package (VASP).[19] Electron–ion interactions were described with the projector augmented-wave (PAW) method.[20] The exchange–correlation energy was described using the PBE functional.[21] Dispersion interactions were included using Grimme's D3 correction.[22] The k-point mesh was generated with a VASPKIT k-point density of 0.04 (2π Å^{-1}).[23] A plane-wave kinetic-energy cutoff of 450 eV was used. Electronic and ionic relaxations were converged to 1e-5 eV and -0.02 eV·Å^{-1}, respectively. Spin polarization was included throughout. For slab models, a vacuum region of ~15 Å was introduced along the surface-normal direction. During slab relaxations, the bottom 1 layer was fixed while the remaining atoms were relaxed. On-site Coulomb interactions were treated within the DFT+U framework using the Dudarev approach (U_eff = U − J), with U_eff values of Co: 3.52 eV.[24] Post-processing and data analysis were carried out using VASPKIT.[23] Adsorption energies were calculated as $E_{ads} = E_{surf+ads} - E_{surf} - E_{adsorbate}$, where $E_{surf+ads}$ is the total energy of the adsorbate–surface system, E_{surf} is the clean-surface energy, and $E_{adsorbate}$ is the isolated adsorbate energy.

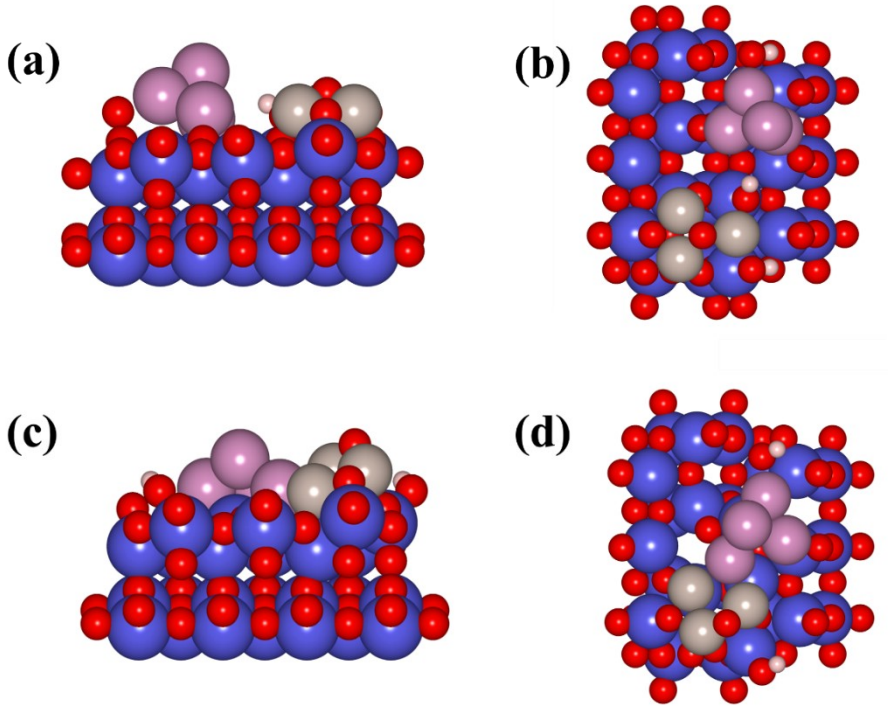

Fig. S22 Side and top views of Ru-Co/TiO_2 (a and b) and Ru-Co/TiO_{2-x}-500 model (c and d) for Bader charge analysis.

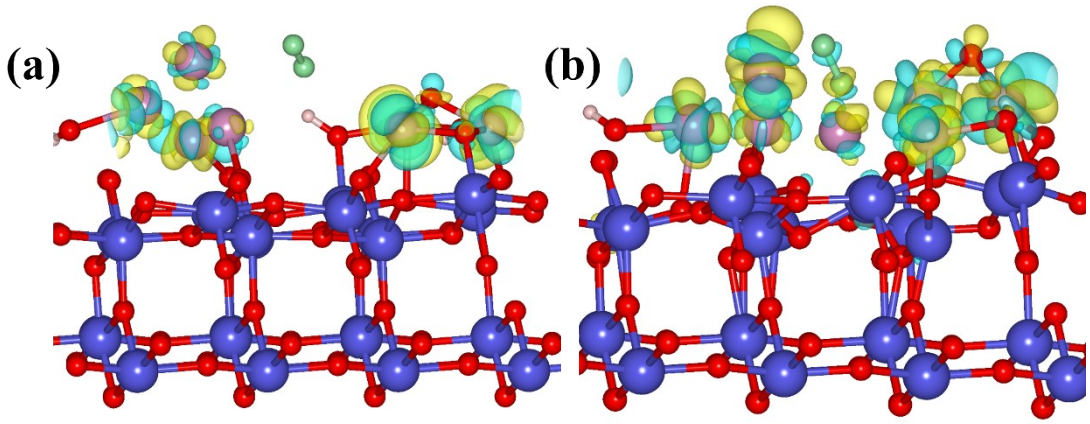

Fig. S23 The optimized adsorption configurations of N_2 molecules with their corresponding charge distribution on the surface of (a) Ru-Co/TiO_2, and (b) Ru-Co/TiO_{2-x}-500 catalysts.

References

(1) Li, S.; Shao, Y.; Chen, H.; Fan, X. Nonthermal Plasma Catalytic Ammonia Synthesis over a Ni Catalyst Supported on MgO/SBA-15. *Ind. Eng. Chem. Res.* **2022**, *61* (9), 3292–3302. https://doi.org/10.1021/acs.iecr.1c04968.

(2) Luo, S.; Liu, Y.; Song, Y.; Yang, Y.; Chen, F.; Chen, S.; Wei, Z. Plasma-Induced Nitrogen Vacancy-Mediated Ammonia Synthesis over a VN Catalyst. *Chem. Commun.* **2024**, *60* (24), 3295–3298. https://doi.org/10.1039/D4CC00042K.

(3) Bajpai, A.; Kumar, S. Tailoring the Surface Acidity of Catalyst to Enhance Nonthermal Plasma-Assisted Ammonia Synthesis Rates. *Mol. Catal.* **2024**, *557*, 113961. https://doi.org/https://doi.org/10.1016/j.mcat.2024.113961.

(4) Nguyen, H. M.; Gorky, F.; Guthrie, S.; Carreon, M. L. Sustainable Ammonia Synthesis from Nitrogen Wet with Sea Water by Single-Step Plasma Catalysis. *Catal. Today* **2023**, *418*, 114141. https://doi.org/https://doi.org/10.1016/j.cattod.2023.114141.

(5) Li, X.; Jiao, Y.; Cui, Y.; Dai, C.; Ren, P.; Song, C.; Ma, X. Synergistic Catalysis of the Synthesis of Ammonia with Co-Based Catalysts and Plasma : From Nanoparticles to a Single Atom. **2021**. https://doi.org/10.1021/acsami.1c12695.

(6) Liu, Y.; Xu, X.; Song, Q.; Guo, Z.; Wu, X.; Chen, C.; Chen, Q.; Zhang, H. Co-Ni/MOF-74 Catalyst Packed-Bed DBD Plasma for Ammonia Synthesis. *Plasma Process. Polym.* **2024**, *21* (2), 2300086. https://doi.org/https://doi.org/10.1002/ppap.202300086.

(7) Li, S.; van Raak, T.; Gallucci, F. Investigating the Operation Parameters for Ammonia Synthesis in Dielectric Barrier Discharge Reactors. *J. Phys. D. Appl. Phys.* **2020**, *53* (1), 014008. https://doi.org/10.1088/1361-6463/ab4b37.

(8) Mizushima, T.; Matsumoto, K.; Sugoh, J.; Ohkita, H.; Kakuta, N. Tubular Membrane-like Catalyst for Reactor with Dielectric-Barrier-Discharge Plasma and Its Performance in Ammonia Synthesis. *Appl. Catal. A Gen.* **2004**, *265* (1), 53–59. https://doi.org/https://doi.org/10.1016/j.apcata.2004.01.002.

(9) Zhang, Y.; Li, S.; Qiu, B.; Chen, S.; Chen, H.; Fan, X. MgAl Layered Double

Hydroxide (LDH) for Promoting Ammonia Synthesis in Non-Thermal Plasma: Role of Surface Oxygen Vacancy. *Chem. Eng. Process. - Process Intensif.* **2024**, *195*, 109608. https://doi.org/https://doi.org/10.1016/j.cep.2023.109608.

(10) Kim, H.-H.; Teramoto, Y.; Ogata, A.; Takagi, H.; Nanba, T. Atmospheric-Pressure Nonthermal Plasma Synthesis of Ammonia over Ruthenium Catalysts. *Plasma Process. Polym.* **2017**, *14* (6), 1600157. https://doi.org/https://doi.org/10.1002/ppap.201600157.

(11) Gao, B.; Cao, G.; Hu, D.; Guo, L.; Ba, Z.; Li, C.; Zhao, J.; Fang, Y. Insight into the Effect of Support Properties on DBD Plasma-Catalytic NH3 Synthesis over Ru-Co Bimetallic Catalysts. *Fuel* **2025**, *382*, 133802. https://doi.org/https://doi.org/10.1016/j.fuel.2024.133802.

(12) Ye, B.; Liu, C.; Chen, Y.; Chen, Q.; Jing, K.; Yu, J. C.; Wu, J.; Wu, L. Regulating the Unsaturated Co Sites on MOF-74(Co) for Enhancing Photocatalytic N2 to NH3 Conversion. *ACS Sustain. Chem. Eng.* **2025**, *13* (9), 3588–3599. https://doi.org/10.1021/acssuschemeng.4c09653.

(13) Song, S.; Wang, F.; Sun, X.; Chen, Y.; Liu, J.; Shi, Y.; Ning, P.; Ma, Y.; Li, K. Plasma-Assisted Ammonia Synthesis from N2 and H2O over RGO-TiO2 Catalysts: Enhancing Energy Efficiency and Unraveling Reaction Mechanisms. *ACS Catal.* **2025**, *15* (20), 17603–17613. https://doi.org/10.1021/acscatal.5c06041.

(14) Yuan, J.; Feng, W.; Zhang, Y.; Xiao, J.; Zhang, X.; Wu, Y.; Ni, W.; Huang, H.; Dai, W. Unraveling Synergistic Effect of Defects and Piezoelectric Field in Breakthrough Piezo-Photocatalytic N2 Reduction. *Adv. Mater.* **2024**, *36* (5), 2303845. https://doi.org/https://doi.org/10.1002/adma.202303845.

(15) Wang, L.; Yi, Y.; Zhao, Y.; Zhang, R.; Zhang, J.; Guo, H. NH3 Decomposition for H2 Generation: Effects of Cheap Metals and Supports on Plasma–Catalyst Synergy. *ACS Catal.* **2015**, *5* (7), 4167–4174. https://doi.org/10.1021/acscatal.5b00728.

(16) Lv, L.; Chu, P.; Han, T.; Jiang, Y.; Wang, Z.; Liu, Y.; Dai, H.; Wei, L.; Deng, J. Carbon and Oxygen Double Defects-Enhanced Ru-Based Catalyst for Ammonia

Decomposition. *Angew. Chemie Int. Ed.* **2025**, *64* (23), e202501898. https://doi.org/https://doi.org/10.1002/anie.202501898.

(17) Winter, L. R.; Ashford, B.; Hong, J.; Murphy, A. B.; Chen, J. G. Identifying Surface Reaction Intermediates in Plasma Catalytic Ammonia Synthesis. *ACS Catal.* **2020**, *10* (24), 14763–14774. https://doi.org/10.1021/acscatal.0c03166.

(18) Wang, Y.; Yang, W.; Xu, S.; Zhao, S.; Chen, G.; Weidenkaff, A.; Hardacre, C.; Fan, X.; Huang, J.; Tu, X. Shielding Protection by Mesoporous Catalysts for Improving Plasma-Catalytic Ambient Ammonia Synthesis. *J. Am. Chem. Soc.* **2022**, *144* (27), 12020–12031. https://doi.org/10.1021/jacs.2c01950.

(19) Hafner, J. Ab-Initio Simulations of Materials Using VASP: Density-Functional Theory and Beyond. *J. Comput. Chem.* **2008**, *29* (13), 2044–2078. https://doi.org/https://doi.org/10.1002/jcc.21057.

(20) Blöchl, P. E. Projector Augmented-Wave Method. *Phys. Rev. B* **1994**, *50* (24), 17953–17979. https://doi.org/10.1103/PhysRevB.50.17953.

(21) Perdew, J. P.; Burke, K.; Ernzerhof, M. Generalized Gradient Approximation Made Simple. *Phys. Rev. Lett.* **1996**, *77* (18), 3865–3868. https://doi.org/10.1103/PhysRevLett.77.3865.

(22) Grimme, S.; Antony, J.; Ehrlich, S.; Krieg, H. A Consistent and Accurate Ab Initio Parametrization of Density Functional Dispersion Correction (DFT-D) for the 94 Elements H-Pu. *J. Chem. Phys.* **2010**, *132* (15), 154104. https://doi.org/10.1063/1.3382344.

(23) Wang, V.; Xu, N.; Liu, J.-C.; Tang, G.; Geng, W.-T. VASPKIT: A User-Friendly Interface Facilitating High-Throughput Computing and Analysis Using VASP Code. *Comput. Phys. Commun.* **2021**, *267*, 108033. https://doi.org/https://doi.org/10.1016/j.cpc.2021.108033.

(24) Dudarev, S. L.; Botton, G. A.; Savrasov, S. Y.; Humphreys, C. J.; Sutton, A. P. Electron-Energy-Loss Spectra and the Structural Stability of Nickel Oxide: An LSDA+U Study. *Phys. Rev. B* **1998**, *57* (3), 1505–1509. https://doi.org/10.1103/PhysRevB.57.1505.